Microscopic study on characteristic decorative black and white porcelain produced in Shanxi province, Jin and Yuan dynasties (AD 1115–1368), China

Minli Wang, Christophe Faulmann, Fen Wang, Tian Wang, Philippe Sciau

Microscopic Study on Characteristic decorative Black and White Porcelain produced in Shanxi province, Jin and Yuan dynasties (1115-1368 AD), China

Minli Wang,[1] Christophe Faulmann,[1] Fen Wang,[2] Tian Wang,[2*] and Philippe Sciau[1,2*]

[1] CEMES, UPR CNRS 8011, Toulouse University, 29 rue Jeanne Marvig, Toulouse 31055, France
[2] School of Conservation Science & Technology for Cultural Heritage, School of Material Science and Engineering, Key Laboratory of Materials & Technology for Underground Cultural Heritage Conservation, Ministry of Education, Shaanxi University of Science and Technology, Xi'an 710021, China

Abstract: Black and white porcelain plays a critical role in Chinese decorative porcelain history. It is famous for its decorative styles and techniques, which create a strong black and white color contrast in its appearance. In this study, representative black and white porcelains produced in Shanxi province were analyzed by X-ray fluorescence, Raman spectroscopy and SEM-EDS. The results show that both Ca-rich (~5.33 wt%) and Ca-poor (~1.99 wt%) glazes were used leading to quite different microstructures. The pigment particles of Ca-rich glazes are characterized by small size (≤2 μm), wide distribution, and tightly wrapped by anorthite. In contrast, they are larger (≥2 μm) and tightly cumulated together in Ca-poor glazes. Hematite is the major crystal in pigment, double-substituted by Al and Ti. The Al/Fe ratios are similar, but Ti/Fe ratios are quite different: they do not exceed 0.03% in Ca-poor glazes, whereas they reach 0.12% in Ca-rich glazes, suggesting that the origin of the pigments must be different. Al-rich mineral such as kaolin was added to the pigment preparation in Ca-rich glazes. The color of the pattern is mainly influenced by the size, quantity and concentration of brown Ti-doping hematite, as well as the thickness of the glaze layer and other crystals and Fe ions. The fired atmosphere of Ca-rich glaze type seems less oxidizing than for Ca-poor glaze type. Overall, the results confirm that black and white porcelain has a variety of production techniques, which is attributed to the craftsman adjusting the techniques according to the composition of raw materials.

Keywords: Black and white porcelain; multilayered structure; hematite (α-Fe_2O_3); Raman spectroscopy; SEM-EDS

1 Introduction

Black and white porcelain, a kind of decorative ware popular in the Jin and Yuan Dynasties (1115-1368 AD),[1] was invented by craftsmen who perfectly incorporated paintings and calligraphy as decorative motifs on white supports.[2] Black and white

porcelain is presently considered as the most typical and characteristic product of decorative Chinese porcelain, with its vivid and realistic design, based on a strong folk style.[3] The development of black and white porcelain reached its peak during the Jin Dynasty with the manufacturing of many exquisite works for foreign markets. More importantly, it is believed that the implementation of new decoration processes influenced the development of other decorated porcelains such as red and green porcelains or blue and white porcelain to some extent.[4,5]

The production of black and white porcelain is a crucial stage in the development of Chinese decorated porcelain. It is because it inherited the decorative techniques of black and white porcelain figurines from the Sui Dynasty (581-619 AD). On this basis, it developed a unique decorative style and exquisite craftsmanship, which greatly influenced the creation and development of blue and white porcelain in the Yuan dynasty (1271-1368 AD) and beyond. The development of black and white porcelain stimulated the emergence of a rich array of decorative techniques and thematic motifs, to a certain extent, encapsulating the prevailing socio-economic and cultural milieu of that era. Black and white porcelain has a rich variety of decorative techniques, it is usually categorized into three types depending on the location of the decoration, [6] as shown in Fig. S1, (a) over-glazed decoration: glaze is applied to the body/slip, paint decoration is applied on top of it; (b) under-glazed decoration: decoration is applied directly to the body/slip, then transparent glaze is applied on top of it; (c) inter-layer decoration: glaze is applied to the body/slip, then paint decoration is applied to the body/slip and transparent glaze is applied on top of it after it dries. Brushes are the most common tool used for decoration. Besides, more complex techniques are applied to it, such as carving and inlay, to obtain more elaborate designs.[7]

This key role played by black and white porcelain in the development of decorative techniques has received increasing attention in recent years from researchers. Leung *et al.*[7] characterized the chemical composition of the bodies and glazes, revealing that Fe_2O_3 is the colorant and flux of colored glaze. Jiang *et al.*[4] investigated the chemical formulation and microstructure of black decoration in red and green porcelain, indicating that they are high-temperature underglazes and revealing the evolution of the technology. D. Ma *et al*.[8] performed technical analyses on black and white inlay porcelain, subsequently elucidating the interplay of technologies in Southeast Asia. Moreover, Some archaeologists have pointed out that black and white porcelain to some extent influenced the development of blue and white porcelain in the Yuan and Ming dynasties (1271-1644 AD).[6] However, a comprehensive understanding of the complex structure of black and white porcelain and of the structure and composition of the fugitive crystals in black decoration continues to be explored.

In this study, we combined Raman spectroscopy and scanning electron microscopy to investigate in-depth the microstructure and color-imparting crystals of the black decorations produced in Shanxi province. The samples are categorized into Ca-rich glazes from the Hejin[9] and Xiangning[10] kilns and Ca-poor glazes from the Huozhou[11] kilns based on the Ca concentration in glazes.

2 Materials and Methods

2.1 Sample description and preparation

A preliminary study on 21 black and white porcelain sherds collected from archaeological strata of the Jin-Yuan period (AD 1115-1368) from Hejin, Xiangning, and Huozhou regions has shown that the main differences between the samples are the Ca content and the microstructure**.** Taking these features into account, 4 sherds were selected for this study: 2 sherds with high Ca content GZ-BD01 (Fig.1a) and TGD-BD06 (Fig. 1b) and 2 sherds with low Ca content HZ-BD01 (Fig. 1c) and HZ-BD02 (Fig.1d). The patterns of these fragments are all black according to visual observation. Optical microscopy images of the surfaces under each picture of sherds (Figs.1e-h) show that the patterns are not pure black. GZ-BD01, TGD-BD06 and HZ-BD01 are black-brown (Figs. 1e,1f and 1g, respectively), while HZ-BD02 has the darkest colour (Fig. 1h). More detailed characterization of the samples is described in Table S1.

SEM and Raman spectroscopy measurements were carried out on polished cross-sections. The cross-sections were made by cutting the fragments into small pieces using a diamond cutter, then fixing them in epoxy resin. They were then ground with silicon carbide paper (1200-4000 grit) and polished with micro-diamond paste down to 1 μm. As the samples were not electrically conductive, they were coated with carbon before being examined under a scanning electron microscope.

2.2 Analytical techniques

2.2.1 X-ray fluorescence spectroscopy (XRF)

Elemental composition was measured using the micro-XRF analyzer (Horiba, XGT-7200, Japan). Spectral collection and analysis are performed by the XGT-7200 software equipped with the instrument. The analysis was performed with x-ray tube voltage of 50 kV and a current of 1 A. **Calibration with Corning Glass prior to measurement**. The incident X-ray beam diameter was 1.2 mm and the acquisition time for each spectrum was set to 120 s. The measurements were carried out on surface and at least three spectra were recorded for each zone in order to minimize heterogeneous effects. Mappings were performed on ceramic surfaces (19*19 mm^2) with also a beam diameter of 1.2 mm. All measurement processes were carried out under vacuum conditions.

2.2.2 Scanning electron microscopy and energy dispersive spectrometry (SEM-EDS)

The investigations were performed in Thermo Fisher Helios NanoLab 600i with an acceleration voltage of 15 kV and 18 kV, the current is 0.69 μA, and the working distance between 6~7 mm, the chamber pressure range from $3.12*10^{-4}$ Pa to $5.05*10^{-4}$ Pa. An Oxford instruments EDS detector was used to record the elemental content and distribution, the diameter of the EDS probes is about 0.2 μm, the process time is 4. The data obtained were recorded and processed using AZtec software.

2.2.3 Micro-Raman spectroscopy

The study was performed by Xplora MV 2000 (Horiba Jobin-Yvon) micro-Raman spectroscopy equipped with 532 nm excitation provided by a solid-state laser was performed to analyze the crystals in cross section of the glaze at room

temperature. The laser was focused and scattered light was collected under a 100x objective. The spatial resolution is 1 μm and the laser power is about 1.3 mW. The optimal spectral curve was obtained by the minimum smoothing method. Igor Pro software was used for data fitting.

3 Results

3.1 Elemental composition

The elemental compositions obtained by XRF are given in Table 1, in oxide mass equivalence. For the body, Al_2O_3 (24.35-30.25 wt%) and SiO_2 (59.38-67.15 wt%) are in accordance with the ones the productions of the northern regions. High Fe concentration (~4.46 wt%) is the source of gray/brown bodies. Since the XRF analysis of black decorations and white background was measured from the surface of the fragments and only a fraction of the X-rays penetrated the glaze to reach the pigmented area due to the effect of the upper glassy matrix, so the chemical composition of the black decorations cannot be taken as an accurate composition of the pigment. The major difference between the black decoration and the white background is the Fe content. As the concentrations of Al, Si, K and Ca are very similar, this means that Fe is the main colouring element in the black decoration. An obvious result is that the CaO content in GZ-BD01 (5.13-6.31 wt%) and TGD-BD06 (4.56-5.32 wt%) is significantly higher than in HZ-BD01 (1.42-1.72 wt%) and HZ-BD02 (2.26-2.57 wt%). The Fe_2O_3 content of the HZ-BD02 black decoration is much higher, 19.00 wt%, which can be explained by the fact that the pigment zone is closer to the surface than in the other samples.

As shown in Fig. S2, the XRF mapping images better visualize the elemental distribution on the surface. The distribution of iron elements is consistent with the black pattern. The traces of using brushes can be observed on TGD-BD06, HZ-BD01 and HZ-BD02. In addition, Ti concentration is high in the pattern of TGD-BD06, and almost absent in HZ-BD01 and HZ-BD02.

3.2 Morphological analysis

Fig. 2 shows the multilayer structure of the cross-section of samples as well as the microscopic images of the pigmented areas. The microstructures of black decorations exhibit significant differences. In GZ-BD01, glaze on the top and the pigment area below, with a white reaction layer at their junction (Fig. 2a). In the enlarged image of the pigmented area, the white reaction layer comprises a large number of well-developed needle-like crystals. Beneath it, a substantial gathering of plate-like crystals and irregular particles can be observed (Fig. 2b). In TGD-BD06, a white slip lies between the body and pigment (Fig. 2c). A considerable portion of the glaze layer is occupied by numerous plate-like crystals and irregular particles (Fig. 2d). The glaze of HZ-BD01 and HZ-BD02 is very thin (Fig. 2e and 2g, respectively), with a large number of tightly packed large irregular crystals in the pigment area (Fig. 2f and 2h, respectively). Needle- and plate-like crystals are not observed in the pigment of either HZ-BD01 or HZ-BD02. In addition, large crystals with melted edges were observed in the glazes of TGD-BD06, HZ-BD01, and HZ-BD02 (crystals marked with yellow circles in Figs. 2d, 2f, and 2h, respectively). Interestingly, HZ-

BD01 and HZ-BD02 feature a thin layer of approximately 25 μm between the pigment layer and the white slip.

The crystallization zones of the samples exhibit some similarities. Specifically, the crystallization zones of GZ-BD01 and TGD-BD06 feature small and dispersed crystals surrounded by plate-like crystals, while the crystallization zones of HZ-BD01 and HZ-BD02 share similarities in crystal size and morphology. Consequently, we chose to further investigate the crystallization regions of TGD-BD06 and HZ-BD01, as shown in Fig. 3. In TGD-BD06 (Fig. 3a), plate-like crystals are well developed, and elemental mapping suggests that they are rich in Al (Fig. 3c) and Ca (Fig. 3d). Besides, a large aggregation of needle-like crystals contains Al (Fig. 3c). An enlargement image is shown Fig. S3a. EDS analysis of individual crystals revealed that the Al concentration is about 26.5 wt% (Fig. S3b). Fig. 3e and 3f show that these irregular crystals contain high Fe concentration and low Ti concentration. In HZ-BD01 (Fig. 3g), there is no plate-like crystals rich in Al (Fig. 3i) and Ca (Fig. 3j) formation other than irregular-shaped crystals (2-8 μm) at the interface between the white slip and the glaze layer. However, as shown in Fig. 3g, a high concentration of Al is below the pigment layer (corresponding to the thin layer between the pigment and makeup clay in Fig. 2e). Upon image magnification, it is found that this area consists of many needle-like crystals (Fig. S3c), and the EDS results show that the Al content of the crystal is approximately 25.3 wt% (Fig. 2d). Fig. 3k and 3l show that these crystals are also Fe-rich and contain a low Ti concentration.

These irregular crystals were analyzed by EDS to obtain their chemical composition. In order to avoid the influence of glassy matrix, only large-sized particles (≥2 μm) were measured. The results are expressed in atomic percent (Table 2). Whatever the sample, Fe concentration is similar in all crystals, range from 26.97-33.35 atom%, but the concentration of Ti in the particles from zone 1 (1.32-2.28 atom %) is significantly higher than that of zone 2 (0.22-0.23 atom%).

The microstructure of the cross-section at the interface between black decoration and white glaze is investigated, as shown in Fig. 4. In GZ-BD01, numerous needle-like and plate-like crystals were observed both in black decoration and white glaze, but there is no white slip in the black decoration area (Fig. 4a). For the three other samples, there is a clear difference in the distribution and number of crystals at the junction of the black decoration and the white glaze. In TGD-BD06 black decoration (Fig. 4b), a large number of needle-like crystals and iron particles occupy most of the area in the glaze, whereas in the white background, only needle-like particles are formed at the interface between the glaze and the slip. In HZ-BD01 (Fig. 4c) and HZ-BD02 (Fig. 4d), we observe irregular particles in black decoration but no needle-like crystals: only a small number of plate-like crystals are observed at the interface in the white background area.

3.3 Micro-Raman spectroscopy analysis

We investigated the structure of the upper glazes in black decorations, as illustrated in Fig. S4, and their Raman spectra exhibit two broad bands at ~480 cm^{-1} and ~1000 cm^{-1}, corresponding to the bending and stretching vibrations of the SiO_4 tetrahedra, respectively. These characteristics align with the Raman spectral features

of the silicate glass phases found in ancient porcelain glazes.[12] A noticeable difference is the relative intensities and areas (A500/A1000) of the bending and stretching modes in the spectra of GZ-BD01 and TGD-BD06, which are significantly higher than those of HZ-BD01 and HZ-BD02. This difference may be attributed to the high concentration of Ca in the GZ-BD01 and TGD-BD06 glazes.[13]

Crystallographic identification of the crystals labeled in Figs. 3a and 3g (pt01 to pt07) resulted in the characteristic bands of the 7 crystals shown in Figs. 3b and 3h. Fig. 3b shows that the Raman bands of pt01, pt02 and pt03 in zone 1 are located at about 223, 295, 414, 618, 668 and 1333 cm^{-1}, which are the typical Raman bands for hematite[16]. It has been checked that hematite has not been generated from oxides by thermal effect by using a lower power for the Raman experiment: the spectra have also been recorded with a lower power of 0.08 mW, it exhibits the same bands, but less defined and much noisier (Fig. S5). Crystal pt04 is identified as anorthite because of the 189, 280, 482, 505 and 558 cm^{-1} bands. Fig. 4h also shows that pt05, pt06, and pt07 are hematite crystals, but there is no anorthite formation. As shown in Fig. 5, in addition to the large amount of hematite in zone 1, spinel and pseudobrookite crystals are also formed in other black-decorated areas of TGD-BD06.

To investigate the effect of ion doping on the crystal structure of hematite, the elemental compositions and corresponding Raman spectra of hematite crystals were measured in different areas of the Ca-rich glaze GZ-BD01, TGD-BD06 and the Ca-poor glaze HZ-BD01, HZ-BD01, respectively. The deconvolution calculation of the Raman spectra was performed to get the displacement and half-height widths of the strong spectral bands at about 670 cm^{-1}. It should be noted that the measured hematite crystals are larger than 5 μm in size, thus minimizing the influence of the glass matrix on the measurements. As shown in Fig. 6, a double substitution of Ti and Al ions is formed in the hematite structure. Fig. 6a and 6b show the trend of Ti and Al doping on the position of the 670 cm^{-1} band, respectively. Fig. 6a shows that Ca-rich glazes GZ-BD01 and TGD-BD06 have slightly higher Ti-doping in hematite than Ca-poor glazes HZ-BD01 and HZ-BD02. This band also shifts towards lower wavenumber with increasing Ti-doping, whereas it tends to shift to higher wavenumber with increasing Al-doping (Fig. 6b). In Fig. 6c, it is shown that with an increase in the Ti-doping concentration, the FWHM (full width at half maximum) of the band exhibits a nearly linear trend of augmentation. In Fig. 6d, the Al doping concentration appears to exhibit no pronounced correlation with the broadening of the 670 cm^{-1} band. Under equivalent levels of Al-doping, the spectral band broadening of GZ-BD01 and TGD-BD02 exceeds that of HZ-BD01 and HZ-BD02.

4 Discussion

As observed in the results section, Ca-rich glaze and Ca-poor glaze samples exhibit numerous differences not only in micro-structure but also in the chemical composition related to elements other than Ca. These discrepancies can be attributed to disparities in raw materials and the manufacturing processes employed.

Considering the positioning of the black pigment layer, GZ-BD01 and TGD-BD06 are both under-glazed decorations because their pigments are between the body/slip and the transparent glaze. The process involves covering the raw body with a variable thickness layer of white slip, waiting for it to dry, then painting with brushes dipped in black pigment and covering it with a layer of transparent glaze before firing at high temperature. GZ-BD01 has a more complex process involves carving the design into the white slip and filling it with pigment before glazing it, resulting in a sharper effect.

The pigment layer of HZ-BD01 and HZ-BD02 is also underneath the transparent glaze, but seems to have a more complex structure. It is noteworthy that there is a ~25 μm layer between the pigment and white slip. The elemental distribution shows that this layer is enriched in aluminum as well as small amounts of calcium and potassium compared to the transparent glaze, while the silicon concentration is significantly lower (Fig. S6). The composition of the glass matrix encapsulating the iron particles is very similar to that of the upper transparent glaze (Table S2), which implies that a glaze liquid may have been added to the pigments. Enlargment image shows that only a large number of mullite particles are observed below the pigment (Fig. S3c and S3d). Its formation is facilitated by the melting of pigments at high temperatures accompanied by diffusion of iron ions into the white slip, while aluminum ions migrate from white slip along the concentration, thus promoting the growth of mullite at the interface. The layer is therefore most likely formed by the reaction between the pigment and the white slip during the firing stage, its thickness are related to the firing temperature and duration.

The high Ca concentration in the GZ-BD01 and TGD-BD06 glazes (4.56-6.31 wt %) provides sufficient material conditions for the formation of anorthite. Ca^{2+} readily reacts with Al^{3+} to form a dense layer of anorthite crystals at the body/slip-glaze interface. Therefore, large amounts of well-developed anorthite crystals in the pigment are formed in-situ. Moreover, glazes with a high Ca concentration are less viscous and easier to flow at high temperatures, which leads to pigment diffusing into the glassy matrix. Therefore, Al-rich minerals or the addition of kaolin to black pigments are applied to prevent the diffusion of pigment. This technique is similar to that used for cobalt blue pigments of blue and white porcelain produced during the Ming and Qing dynasties.[17]

Although the high concentration of Ca in the upper glaze facilitates the flow of the glassy phase, the high concentration of Al in the pigment increases its viscosity at high temperatures,[18,19] making it less likely to flow with the glaze, leading to the formation of a large number of anorthite crystals in the pigmented areas. This explains the significant difference in the distribution of anorthite between the regions of the white background and the black decoration. On the contrary, the Ca contents in HZ-BD01 and HZ-BD02 are lower than that of GZ-BD01 and TGD-BD06, and there is a slight decrease in the concentrations of MgO and Na_2O, while K_2O content does not change. Theoretically, the reduction of fluxes such as CaO and MgO leads to an increase in glaze viscosity.[1,20] Therefore, there is no need to use aluminum-rich pigments in Ca-poor glazes to ensure the sharpness of the patterns. Moreover, Ca is a

modifier of the glass network, breaking the Si-O bonds and altering the degree of polymerization. Consequently, the higher Ca concentration results in lower relative intensities (A500/A1000) of the Si-O bending and stretching modes,[14,15] this explains the difference in Raman spectra of black decorations of Ca-rich and Ca-poor glazes (Fig. S4). It can be inferred that the craftsmen in Shanxi Province were able to select different pigment sources and to adjust their processes according to the composition of the glazes to their composition.

In the black decoration of the Ca-rich glaze samples, although the presence of numerous hematite crystals indicates that they were mainly fired in an oxidizing atmosphere. Spinel phase is also detected (Fig. 5), the EDS results indicate Fe content is 15.78 atom%, Ti content is 1.23 atom%, and Al content is 6.88 atom% (Table S3). Consequently, the crystal in question may be identified as an iron spinel, with the possibility of some Fe atoms being substituted by Al and Ti. Given that magnetite can form from hematite in a reducing atmosphere, we can assume that the atmosphere was not totally oxidizing, or at least unstable. During this transformation, the color of the initial hematite changes to earthy brown or even black, probably due to elemental substitution.[21] The abundance of pseudobrookite in the pigment area of GZ-BD01 and TGD-BD06 could be attributed to the formation of high concentrations of Fe and Ti in the raw material at elevated temperatures, as suggested in the references.[22,23] It is also observed in ancient Roman Terra Sigillata[24] and Chinese oil spotted glaze,[25] Alternatively, it's possible that pseudobrookite is inherently present in the raw material itself, as it is known to be highly stable and does not completely decompose until temperatures as high as 1300 °C. [26]Therefore, the large stable pseudobrookite crystals in the pigment area suggest that the porcelain may have been fired at temperatures lower than 1300 °C. Furthermore, the crystal types in Ca-poor glazes HZ-BD01 and HZ-BD02 are relatively simple, consisting primarily of hematite and unmelted particles, identified as quartz crystals (Fig. S7). The large amount of hematite crystals suggests that the atmosphere up to the glaze vitrification was oxidizing.

The hematite crystals in this study are substituted with Al and Ti. The strong band around 670 cm^{-1} observed in Raman spectroscopy is not present of pure hematite.[27] It can be attributed to (i) the superimposition effect of magnetite;[28,29] (ii) the breaking of lattice symmetry caused by Al[27,30]and Ti[31] doping, thermal treatment, weathering, etc; (iii) finite-size effects in nanocrystalline hematite.[16,29] Previous studies have shown that Al-doping will lead to the appearance of the 670 cm^{-1} band, but its intensity is low.[30,32] Therefore, we speculate that this band is most likely produced by the substitution of Al ions and Ti ions, these ions change the color of hematite. Al-doping lightens the color of hematite[33,34] but Ti-doping may change hematite crystals to brownish red color.[25]

Scatter plots of Ti and Al doping versus the around 670 cm^{-1} band (Fig. 6) illustrate that the relationship between the amount of ion doping and the shift of the peak position is complex and is not determined by a single ion doping. However, there is a clear relationship between Ti-doping and the FWHM of this band, rather than Al. Since the radius of Ti^{4+} (0.61 Å) is slightly smaller than the radius of Fe^{3+}

(0.65 Å), Fe^{3+} in the hematite lattice is easily replaced by Ti^{4+}, forming a highly polarizable Ti-O bond.[35,36] But in order to maintain the charge balance inside the hematite crystal, another Fe^{3+} must be converted into Fe^{2+}. The more Ti-doping, the more hematite structure disordered, which is consistent with the result that the FWHM of the band increases with the increase of Ti-doping concentration.

Based on the positioning of the black pigment within the glaze layer, both Ca-rich glaze and Ca-poor glaze samples fall under the category of under-glazed decoration. A delicate white slip covers dark and rough objects to enhance the contrast between black and white colors. Additionally, Al-rich pigments are used in the decoration of Ca-rich glazes, while higher purity iron ores are used for decoration in Ca-poor glazes.

The color of black decorations is affected by the categories, size, and quantities of crystals, as well as the valence and concentration of the color-imparting ions in the glass phase. We find that the pattern is darker in areas where the pigment layer is thicker. Hematite, the major color-imparting crystal, changes from red to brown due to Ti doping. Hematite is small in size and quantity, the glaze is thicker and has a large number of anorthite crystals, and a large number of magnetite particles are formed, deepening the patterned color of the Ca-rich glaze. In contrast, the hematite crystals in the Ca-poor glaze are larger and more numerous, some of the crystals are exposed on the surface. After the light passes through the extremely thin glaze layer and reaches the densely arranged hematite, it is diffusely reflected, thus deepening the color of the pattern and making it dark brown.

5 Conclusions

The multilayered structure of the black and white porcelains investigated in this study is consistent with the characteristics of underglaze-decorated porcelain, including body, white slip, black pigment and top transparent glaze. Both Ca-poor and Ca-rich glazes were used leading to significant differences in the microstructure. In Ca-rich glazes, large quantities of well-developed anorthite surround iron particles, which is in agreement with a deliberate addition of kaolin into the pigment. The majority of crystal iron oxides found in black decoration are substituted (Ti, Al) hematite. Besides, the categories, size, and distribution of iron particles, as well as different Ti/Fe ratios in the hematite, reveal that different sources of black pigments were certainly appled. Their rather large crystal size and Ti substitution could be the origin of the dark color of the decorations. The presence of Ti in the hematite structure increases the charge transfer between cations and anions leading to an increase in absorption in the visible range, so that the patterns observed by the naked eye is dark brown in color, and the shade of the color is related to the size and number of iron particles in the pigment. A large number of tiny magnetite particles was also observed but only in Ca-rich glaze samples.

Acknowledgments

This work has been financially supported by China National Natural Science Foundations (Nos. 62205191), Key Scientific Research Project of Shaanxi Provincial Department of Edu cation (No. 22JY008), Shaanxi Natural Science Basic Research Project (No. 2023WGZJ-YB-45). It was also supported by the China Scholarship Council (CSC). It was performed in the framework of the research collaboration agreement (CNRS No. 186116) between the French National Centre for Scientific Research and the Shaanxi University of Science and Technology.

References

[1] J. Li, *History of Science and Technology of China (Ceramic Volume)*, Science Press, Beijing, 1998.
[2] X. Feng, *Ancient Chinese Ceramics Dictionary*, Cultural Relics Press, Beijing 1998.
[3] Z. Ye, *The History of Chinese Ceramics*, SDX Joint Publishing Company, Beijing 2006.
[4] X. Jiang, Y. Chen, L. Zhang, Z. Zhang, Q. Ma, C. Wang, Y. Yang, *Ceram. Int.* 2017, **43**, 1371.
[5] X. Feng, *Cult. Relics*. 1973, **20**.
[6] D. Qin, *Cult. Relics.* 1994, **48**.
[7] P. L. Leung, M. J. Stokes, C. Tiemei, Q. Dashu, *Archaeometry.* 2000, **42**, 129.
[8] D. Ma, X. F. Zhao, X. C. Y. Jiang, C. S. Wang, W. G. Luo, *Archaeometry.* 2021, ***63***, 1178.
[9] X. Wang, Z. H. Gao, Y. Jia, *Archaeology* 2019, **03**, 48.
[10] Z. Zeng, C. Liu, *World Antiq.* 2017, **9**.
[11] F. Tao, *Archaeol. China* 1992, **522**.
[12] P. Colomban, *J. Non-Cryst. Solids.* 2003, **323**, 180.
[13] P. Colomban, O. Paulsen, *J. Am. Ceram. Soc.* 2005, **88**, 390.
[14] P. Colomban, O. Paulsen, *J. Am. Ceram. Soc.* 2005, **88**, 390.
[15] T. Wang, P. Chen, M. Wang, Z. Sang, P. Zhang, F. Wang, P. Sciau, *J. Eur. Ceram. Soc.* 2020, **40**, 4676.
[16] C. P. Marshall, W. J. B. Dufresne, C. J. Rufledt, *J. Raman Spectrosc.* 2020, **51**, 1522.
[17] X. Jiang, Y. Ma, Y. Chen, Y. Li, Q. Ma, Z. Zhang, C. Wang, Y. Yang, *Spectrochim. Acta. A. Mol. Biomol. Spectrosc.* 2018, **190**, 61.
[18] Y. Iqbal, W. E. Lee, *J. Am. Ceram. Soc.* 2000, **83**, 3121.
[19] Y. Chen, R. Wen, L. Wang, M. Zhang, *Anal. Methods.* 2022, **14**, 541.
[20] T. Zhu, Y. Zhang, H. Xiong, Z. Feng, Q. Li, B. Cao, *Archaeometry.* 2016, **58**, 966.
[21] Z. Jiang, Q. Liu, A. P. Roberts, M. J. Dekkers, V. Barrón, J. Torrent, S. Li, *Rev. Geophys.* 2022, **60**, e2020RG000698.
[22] P. Shi, F. Wang, Y. Wang, J. Zhu, B. Zhang, Y. Fang, *Ceram. Int.* 2017, **43**, 11616.
[23] J.-Y. Kim, H. No, A. Y. Jeon, U. Kim, J.-H. Pee, W.-S. Cho, K. J. Kim, C. M. Kim, C. S. Kim, *Ceram. Int.* 2011, **37**, 3389.

[24] T. Wang, C. Sanchez, J. Groenen, P. Sciau, *J. Raman Spectrosc.* 2016, **47**, 1522.
[25] M. Wang, T. Wang, F. Wang, C. Hole, J. Cao, J. Zhu, P. Zhang, P. Shi, P. Sciau, *J. Raman Spectrosc.* 2022, **53**, 582.
[26] M. Dondi, F. Matteucci, G. Cruciani, G. Gasparotto, D. M. Tobaldi, *Solid State Sci.* 2007, **9**, 362.
[27] F. Froment, A. Tournié, P. Colomban, *J. Raman Spectrosc.* 2008, **39**, 560.
[28] O. N. Shebanova, P. Lazor, *J. Solid State Chem.* 2003, **174**, 424.
[29] D. Bersani, P. P. Lottici, A. Montenero, *J. Raman Spectrosc.* 1999, **30**, 355.
[30] A. Zoppi, C. Lofrumento, E. M. Castellucci, Ph. Sciau, *J. Raman Spectrosc.* 2008, **39**, 40.
[31] F. Rull, J. Martinez-Frias, J. A. Rodríguez-Losada, *J. Raman Spectrosc.* 2007, **38**, 239.
[32] A. Zoppi, C. Lofrumento, E. M. Castellucci, C. Dejoie, Ph. Sciau, *J. Raman Spectrosc.* 2006, **37**, 1131.
[33] H. Hashimoto, J. Kiyohara, A. Isozaki, Y. Arakawa, T. Fujii, J. Takada, H. Inada, T. Takaishi, H. Asoh, *ACS Omega.* 2020, **5**, 4330.
[34] L. Gong, X. Hua, B. Yao, J. Liang, G. Tian, *Ceram. Int.* 2023, **49**, 5066.
[35] A. Wang, K. E. Kuebler, B. L. Jolliff, L. A. Haskin, *Am. Mineral.* 2004, **89**, 665.
[36] R. Rivera, A. Stashans, *Solid State Sci.* 2010, **12**, 1409.

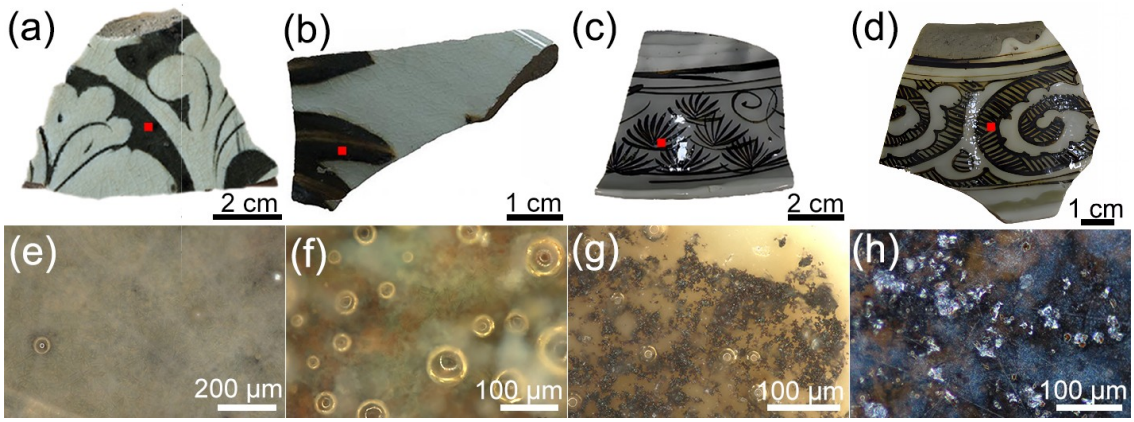

Figure 1 Photographs of four black and white porcelain fragments (a) GZ-BD01;(b) TGD-BD06; (c) HZ-BD01; (d) HZ-BD02 excavated in the southwestern region of Shanxi province and produced in the Jin and Yuan dynasties (1115-1368 AD). The images below each sample correspond to optical microscopy imaging of the surface (labeled as red spots) respectively.

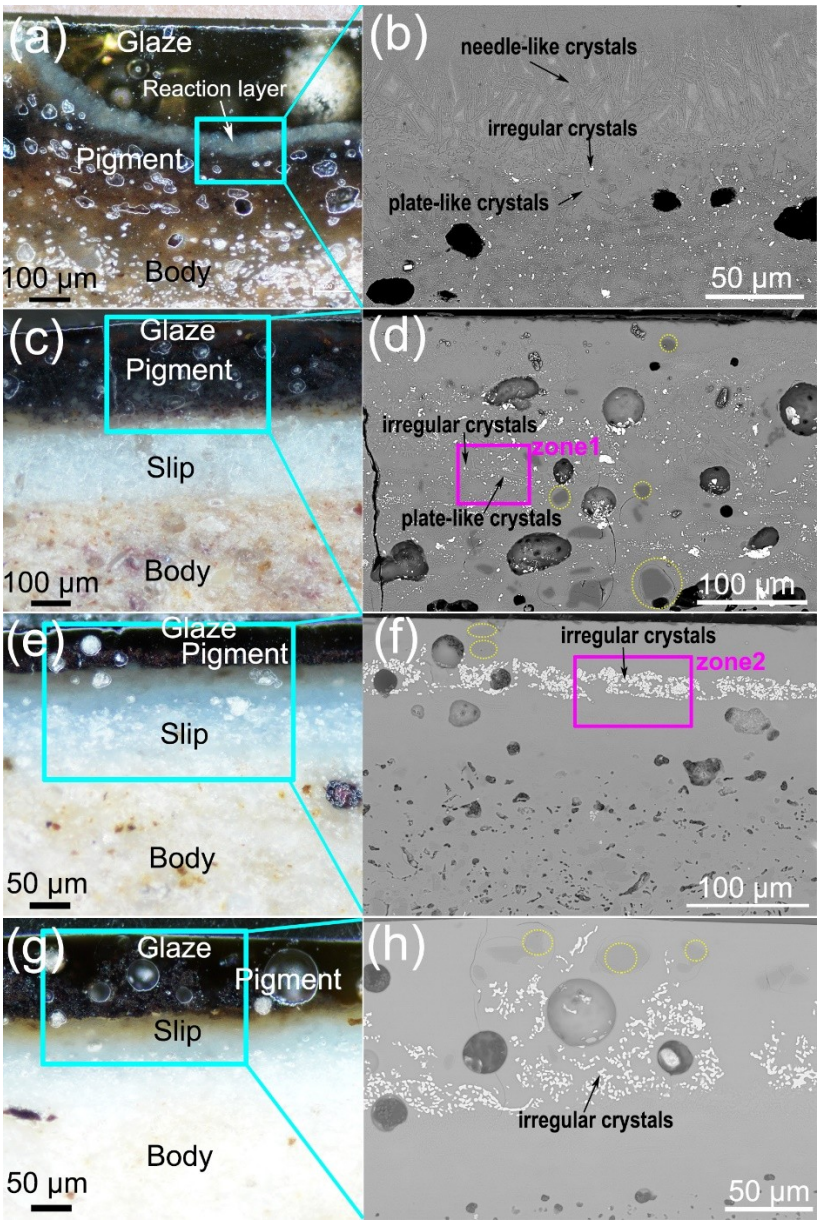

Figure 2 Optical images of the cross-section and SEM images of the corresponding pigment zones of (a and b) GZ-BD01; (c and d) TGD-BD06; (e and f) HZ-BD01; (g and h) HZ-BD02.

Table 1 Analytical results (wt %) obtained by X-ray fluorescence of the four samples.

No.	Component	Na_2O	MgO	Al_2O_3	SiO_2	K_2O	CaO	TiO_2	Fe_2O_3
GZ-BD01	Black decoration	1.22	1.85	16.10	69.53	3.50	5.13	0.21	2.45
	White glaze	0.71	1.59	16.55	70.49	3.15	6.31	0.16	1.05
	Body	0.42	0.38	30.25	59.38	1.94	0.60	1.59	5.44
TGD-BD06	Black decoration	1.18	1.45	15.89	68.51	4.17	4.56	0.27	3.96
	White glaze	1.26	0.82	15.85	72.14	3.65	5.32	0.13	0.83
	Body	0.12	0.28	25.24	65.45	1.39	0.63	1.27	5.61
HZ-BD01	Black decoration	0.71	0.59	15.96	69.83	4.38	1.42	0.17	6.93
	White glaze	0.74	1.05	17.32	73.24	4.39	1.72	0.19	1.35
	Body	0.61	0.45	24.35	67.15	2.31	0.30	1.03	3.80
HZ-BD02	Black decoration	0.28	0.82	14.03	60.07	3.15	2.26	0.31	19.06
	White glaze	0.79	1.31	16.60	72.67	3.83	2.57	0.25	1.99
	Body	0.84	0.53	25.26	66.93	1.84	0.47	1.14	3.00

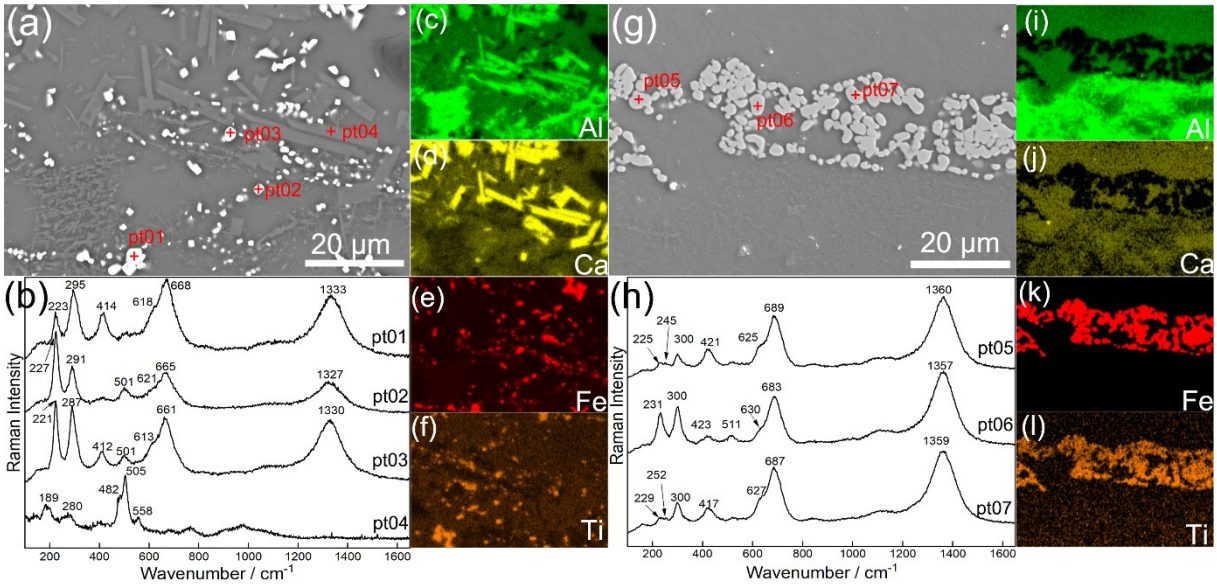

Figure 3 Enlargement SEM images of (a) zone1 in TGD-BD06 and (g) zone2 in HZ-BD01 (magenta rectangles in Figure 2); element mapping of zone1 (c: Al, d: Ca; e: Fe, f: Ti) and (b) Raman spectra recorded on crystals (pt01, pt02 and pt03: hematite, pt04: anorthite) of zone 1; element mapping of zone2 (i: Al, j: Ca; k: Fe, l: Ti) and (h) Raman spectra recorded on crystals (pt05, pt06 and pt07: hematite) of zone 2

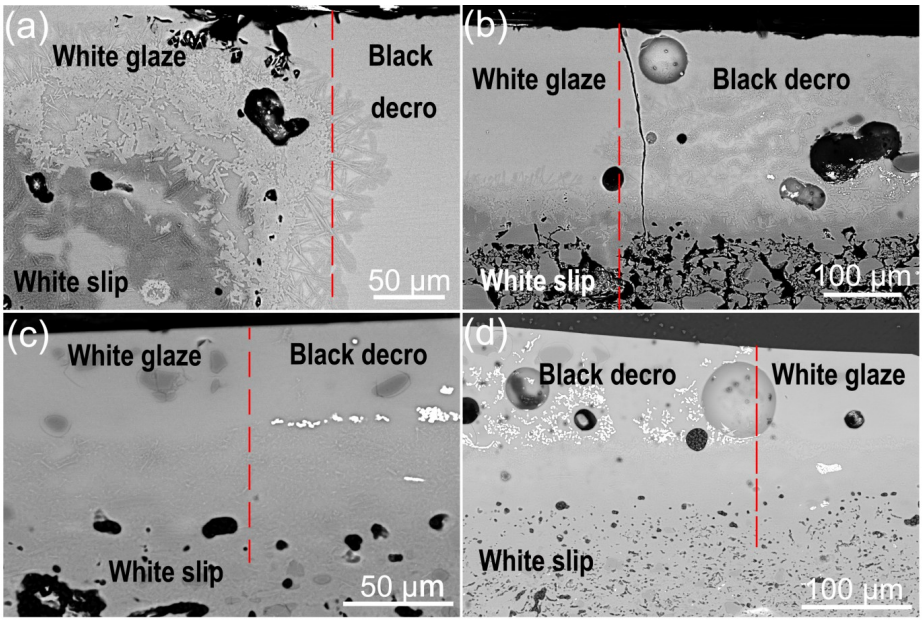

Figure 4 SEM images of the intersection of white glaze and black decoration in cross-section of (a) GZ-BD01; (b) TGD-BD06; (c) HZ-BD01; (d) HZ-BD02

Table 2 EDS spectrum analysis results (atom%) of labeled crystals in Figure 3

	O	Mg	Al	Si	K	Ca	Ti	Fe	Ti/Fe
pt01	59.39	1.20	5.47	1.29	0.31	-	1.32	31.03	0.043
pt02	58.50	0.35	3.99	1.56	-	0.03	2.21	33.35	0.066
pt03	61.58	-	5.69	2.89	0.30	0.28	2.28	26.97	0.085
pt04	62.67	-	15.60	16.05	0.15	5.32	0.20	-	-
pt05	60.58	-	6.00	3.67	0.38	-	0.23	29.00	0.008
pt06	60.78	-	5.69	0.35	-	-	0.23	32.95	0.007
pt07	60.65	-	5.99	0.24	-	-	0.22	32.90	0.007

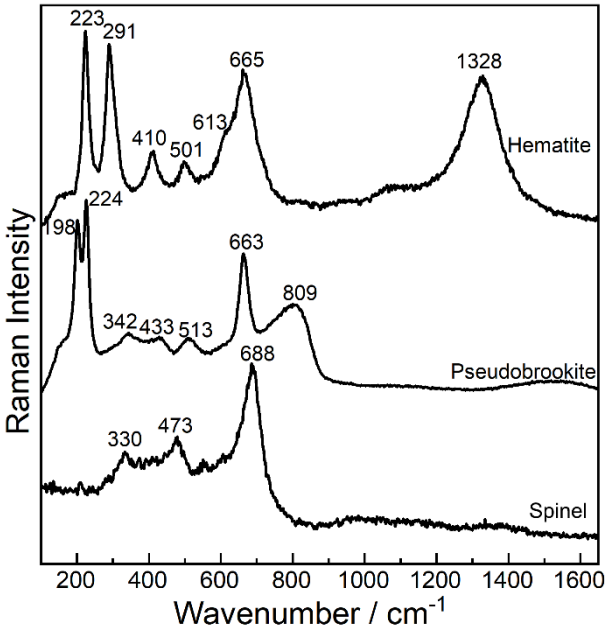

Figure 5 Raman spectra of iron particles collected in the black decorations of Ca-rich glaze TGD-BD06

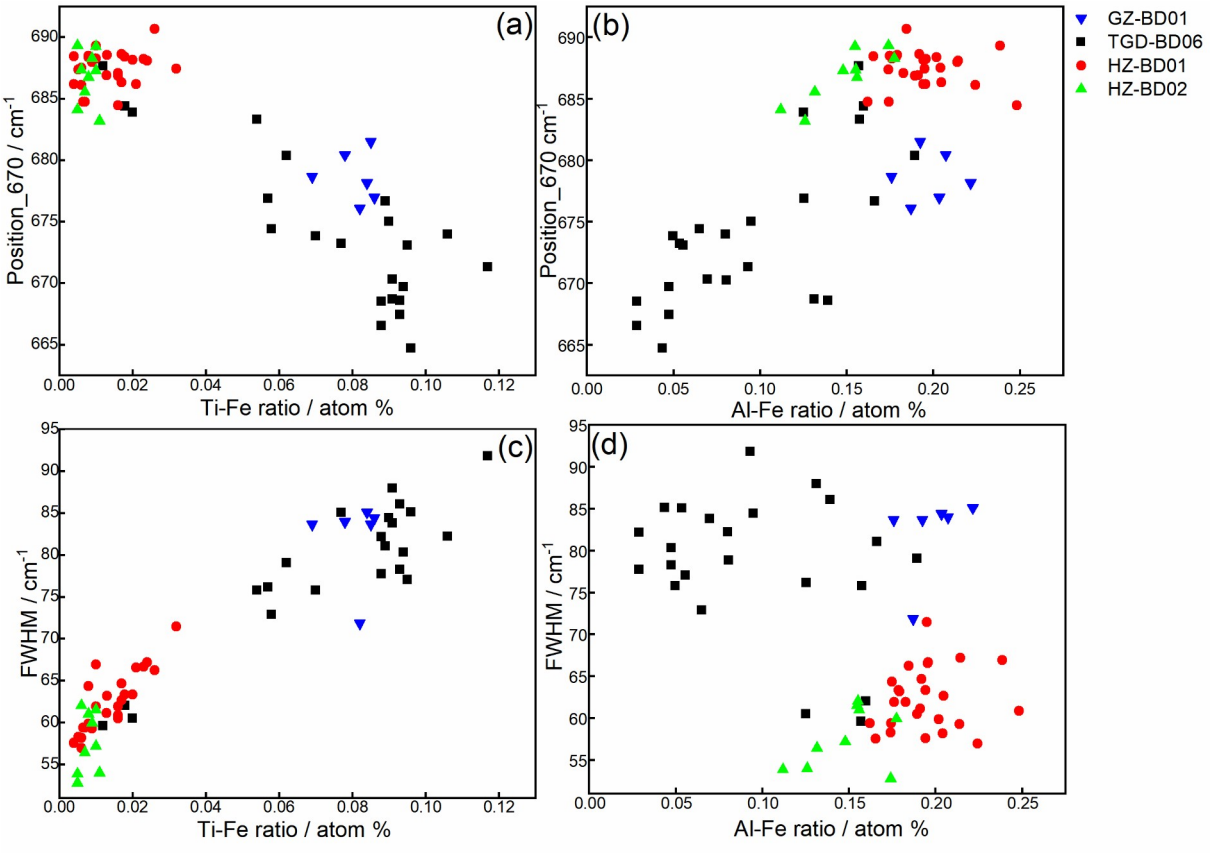

Figure 6 Scatter plots of the 670 cm^{-1} band position in hematite versus (a) Ti/Fe ratio (b) and Al/Fe ratio; Scatter plot of the FWHM (full width at half maximum) of the 670 cm^{-1} band versus (c) Ti/Fe ratio and (d) Al/Fe ratio